Underwater Optical Backscatter Communication using Acousto-Optic Beam Steering

ATUL ROHIT AGARWAL* and DHAWAL SIRIKONDA*, Dartmouth College, USA
ATHARV AGASHE, Dartmouth College, USA
ZIANG REN, Columbia University, USA
DINITHI S. SILVA, Dartmouth College, USA
CHARLES J CARVER, Columbia University, USA
ALBERTO QUATTRINI LI, Dartmouth College, USA
XIA ZHOU, Columbia University, USA
ADITHYA PEDIREDLA, Dartmouth College, USA

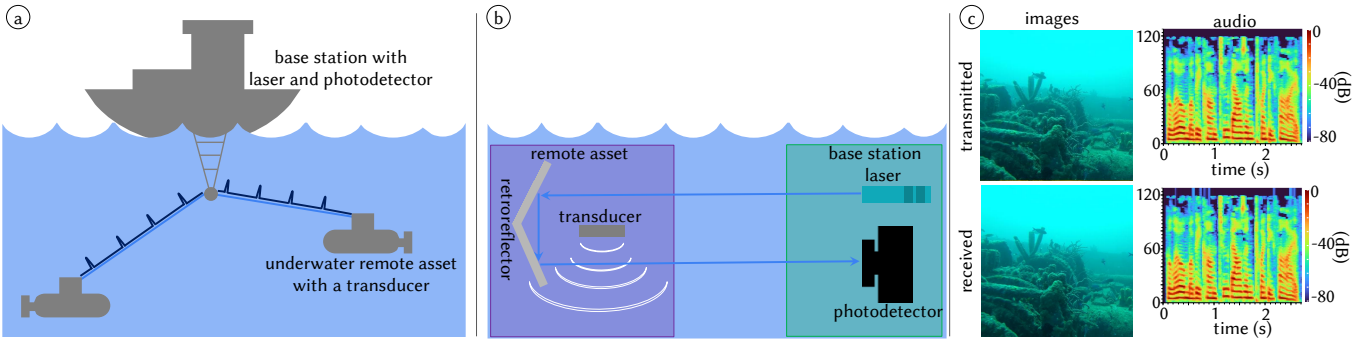

Fig. 1. (a) We introduce an underwater optical backscatter communication method using acousto-optic light steering, enabling data transfer from underwater remote assets to a base station at 0.66 Mbps—orders of magnitude faster than prior underwater or optical backscatter systems. (b) Backscatter systems minimize power use by modulating and reflecting light from an external source (here, the base station) to encode data. Our device uses a retroreflector and ultrasound transducer to steer light: sound waves modulate water's refractive index to direct the beam toward the base station (*bit* 1) or away (*bit* 0). (c) Our prototype transmits various signals reliably at 0.66 Mbps, consuming $\leq$1 µJ/bit, and achieves a bit error rate below 1×10^{-4}—without using error correction.

We present a high-speed underwater optical backscatter communication technique based on acousto-optic light steering. Our approach enables underwater assets to transmit data at rates potentially reaching hundreds of Mbps, vastly outperforming current state-of-the-art optical and underwater backscatter systems, which typically operate at only a few kbps. In our system, a base station illuminates the backscatter device with a pulsed laser and captures the retroreflected signal using an ultrafast photodetector. The backscatter device comprises a retroreflector and a 2 MHz ultrasound transducer. The transducer generates pressure waves that dynamically modulate the refractive index of the surrounding medium, steering the light either toward the photodetector (encoding *bit* 1) or away from it (encoding *bit* 0). Using a 3-bit redundancy scheme, our prototype achieves a communication rate of approximately 0.66 Mbps with an energy consumption of $\leq$1 µJ/bit, representing a 60× improvement over prior techniques. We validate its performance through extensive laboratory experiments in which remote underwater assets wirelessly transmit multimedia data to the base station under various environmental conditions.

CCS Concepts: • **Hardware** → *Wireless devices*; **Emerging optical and photonic technologies**; • **Computer systems organization** → **Optical computing**.

Additional Key Words and Phrases: High-Speed Underwater Wireless Communication, Backscatter Communication, Acousto-Optic Light Steering, Refractive Index Modulation

ACM Reference Format:
Atul Rohit Agarwal, Dhawal Sirikonda, Atharv Agashe, Ziang Ren, Dinithi S. Silva, Charles J Carver, Alberto Quattrini Li, Xia Zhou, and Adithya Pediredla. 2025. Underwater Optical Backscatter Communication using Acousto-Optic Beam Steering. *ACM Trans. Graph.* 44, 6, Article 259 (December 2025), 13 pages. https://doi.org/10.1145/3763289

*Both authors contributed equally to this research.
Project page: https://dartmouth-risc-lab.github.io/aocomm/

Authors' Contact Information: Atul Rohit Agarwal; Dhawal Sirikonda, Dartmouth College, USA, atulrohitagarwal@gmail.com, dhawal.sirikonda.gr@dartmouth.edu; Atharv Agashe, Dartmouth College, USA, atharv.agashe.25@dartmouth.edu; Ziang Ren, Columbia University, USA, zr2272@columbia.edu; Dinithi S. Silva, Dartmouth College, USA, dinithi.s.silva.-.sassaman.gr@dartmouth.edu; Charles J Carver, Columbia University, USA, cjc@cs.columbia.edu; Alberto Quattrini Li, Dartmouth College, USA, alberto.quattrini.li@dartmouth.edu; Xia Zhou, Columbia University, USA, xia@cs.columbia.edu; Adithya Pediredla, Dartmouth College, USA, adithya.k.pediredla@dartmouth.edu.

ACM 1557-7368/2025/12-ART259
https://doi.org/10.1145/3763289

1 Introduction

Effective underwater communication is critical for applications such as remote asset teleoperation, environmental monitoring, and archaeological exploration [Headrick and Freitag 2009; Petillot et al. 2019]. However, existing technologies face fundamental limitations due to the underwater environment [Quattrini Li et al. 2023]. Radio signals attenuate rapidly in water, making them ineffective, while acoustic signals—though widely used—offer limited bandwidth (typically tens of kbps), suffer from multipath interference, and require in-situ calibration due to sensitivity to temperature and pressure.

In contrast, light offers much higher data rates—up to Gbps—and has been demonstrated to support communication over distances of 100 m [Gussen et al. 2016]. However, such high speeds are achievable only with active transmitters. Light-based backscatter systems, which are attractive for low power use, remain constrained to kbps speeds due to slow modulation rates of components like liquid crystals and micromirrors. [Ghiasi et al. 2021; Ghiasi and Zuniga 2024; Wang et al. 2020, 2024; Wu et al. 2020; Xu et al. 2022a, 2023, 2017].

In this manuscript, we introduce a novel underwater optical backscatter communication technique that combines sound and light to enable high-speed, low-power wireless data transmission from remote assets to a base station. Our approach achieves orders-of-magnitude higher throughput than existing solutions, while maintaining energy efficiency ($\leq$1 µJ/bit) and reliability (bit error rate $<1\times10^{-4}$), comparable to state-of-the-art optical backscatter systems (see Tab. 1). Our work builds on Pediredla et al. [2023a] and related research in backscatter communication [Niu and Li 2019].

Similar to existing optical backscatter designs[Shao et al. 2018], we assume a tracking beam from the base station, modulated by the remote asset. Each asset—such as underwater drones, gliders, or static sensor nodes—is equipped with a retroreflector and an ultrasound transducer. The retroreflector sends the tracking beam back to the base station, while the transducer emits sound waves into the water, modulating the tracking beam without optical enclosures.

How is sound encoding data in light? Sound waves create pressure variations in water, dynamically altering its refractive index. These variations act as moving lenses that steer light. We program these lenses to direct the beam toward the detector (*bit* 1) or deflect it elsewhere (*bit* 0), i.e., defocus the beam on the detector.

Theoretically, this technique supports communication rates exceeding 100 Mbps, as acoustic transducers can operate above 500 MHz [Chen et al. 2022, 2017]. Our prototype achieves 0.66 Mbps using a 2 MHz transducer. By comparison, existing optical backscatter methods remain limited to kbps. Note that, while high-frequency ultrasound attenuates within millimeters, in our approach sound is used solely to modulate the reflected light rather than serve as the carrier. Consequently, acoustic propagation is required only across a few millimeters—specifically where the optical beam intersects the pressure field—allowing the method to scale effectively to higher frequencies.

Our method enables the reliable streaming of rich sensor data—such as video, depth maps, and audio—at high bandwidth and low power from underwater cameras and drones. Such capabilities enable digital twins of underwater environments, real-time virtual production, and photorealistic rendering for visual effects, simulation, and interactive media.

Table 1. **Comparison with Optical Backscatter Systems.** We compare our system against prior work based on speed, energy efficiency[2], tested distance (TD), bit error rate (BER), and underwater validation. The **low** BER values indicate $\leq10^{-4}$; **high** indicates $\geq10^{-2}$.

Technique	Speed (kbps)	E/bit (µJ/bit)	TD (m)	BER	Underwater
[Li et al. 2015]	1	0.09	2.4	low	✗
[Xu et al. 2017]	0.25	0.15	$\leq$ 6	high	✗
[Bloom et al. 2019]	0.08	297.5	60	low	✗
[Tapia et al. 2022]	10	11	0.1	low	✗
[Ghiasi et al. 2021]	1	27.4	50	low	✗
[Li et al. 2015]	1	2.69	100	low	✗
[Wu et al. 2020]	8	0.125	7.5	low	✗
[Naeem et al. 2024]	4.8	0.5	5.1	low	✓
Ours (2 MHz)	≈667	1	5.0	low	✓
Ours (39 MHz)	13 000	0.006	5.0	low	✓

To summarize, our key contributions are:

- An underwater optical backscatter communication system using acousto-optic modulation, enabling 0.66 Mbps with a low-cost ($20[1]) 2 MHz transducer, at $\leq$1 µJ/bit and bit error rate below 1×10^{-4}; theoretically scalable to >100 Mbps with 500 MHz devices.
- Experimental validation demonstrating resilience to underwater currents, scattering, and ambient light, using laboratory emulation of these conditions.
- A pathway to further miniaturization and development of compact, field-deployable prototypes.

Overall, this advancement in underwater communication paves the way for broader use of autonomous underwater systems in exploration, infrastructure inspection, and environmental monitoring. At the same time, translating laboratory results into real-world deployments remains a challenge: buoyancy control, water-tight compartments, corrosion, and mechanical stability all impose practical constraints. Our preliminary field trials serve as a case study of these issues, motivating the development of more robust designs and materials for future field-ready prototypes.

2 Related Work

2.1 Underwater Communication

Underwater communication methods fall into two categories: tethered and wireless. Tethered systems, using fiber-optic or copper cables, support throughputs up to 10 Tbps over distances of 10 km [Quattrini Li et al. 2023], but severely limit remote asset mobility.

Among wireless options, acoustic communication is the most established, enabling kilometer-scale distances but offering limited bandwidth—typically up to 10 kbps [Chitre et al. 2008; Eid et al. 2023; Quattrini Li et al. 2023]. Optical transmission systems can achieve higher throughputs, typically 100 Mbps over 100 m and up

[1] As of August 2025
[2] Energy consumed by the transmitter.

to Gbps over shorter ranges [Arnon 2010; Kaushal and Kaddoum 2016; Khalighi et al. 2014; Quattrini Li et al. 2023; Wang et al. 2024], though they require high power and precise alignment. RF-based communication methods are less common, given the high attenuation coefficient of common RF frequencies limiting communication ranges to only a few meters.

Related to purely underwater communication, cross-medium (i.e., air-to-water) communication systems also exist, though they are not very prevalent. Tonolini and Adib [2018] demonstrated a hybrid acoustic-RF design achieving 400 bps, while Carver et al. [2020] extended this to multi-Mbps via optical links. These techniques are later adapted for underwater remote asset positioning using low-throughput optical channels [Carver et al. 2022].

In contrast to these direct transmission techniques, ours is a backscatter communication technique.

2.2 Optical Backscatter Communication

Optical backscatter communication systems reuse existing light (e.g., ambient light from the sun, directional laser light, omnidirectional LED light) and encodes data into light reflections via an external optical modulator (e.g., liquid crystal, digital mirror device), thus eliminating the energy required to create light carrier for communication.

Existing optical backscatter communication techniques are fundamentally constrained by the limited speed of external optical modulators. Most designs use either liquid crystal (LC) shutters [Li et al. 2015; Xu et al. 2017] or fast steering mirrors [Xu et al. 2022b] to encode data onto ambient or directed light. LCs operate via polarization modulation with limited switching speed (at milliseconds) and suffer high optical loss when modulating unpolarized light sources (e.g., sunlight). Steering mirrors modulate by toggling light between an absorber (bit `0`) and a detector (bit `1`).

Several efforts have attempted to optimize performance within these constraints. For instance, Bloom et al. [2019] used LC-based frequency shift keying (FSK) to achieve 80 bps over 4 m indoors and 60 m outdoors. Wu et al. [2019] introduced a Delayed Superimposed Modulation (DSM) scheme exploiting LCD asymmetry, achieving 1 kbps over 6 m. Others have pushed LC-based systems to higher throughput via custom modulation schemes [Ghiasi et al. 2021; Wu et al. 2020; Xu et al. 2022a], enabling kbps-level communication at tens of meters.

Beyond LCs, Wang et al. [2020] demonstrated 1 kbps using polarization-tuned retroreflective signs, achieving communication at µJ/bit energy levels. Tapia et al. [2022] employed spatial modulation to support 10 kbps in a downlink scenario. Xu et al. [2022b] replaced LCs with digital micromirror devices (DMDs), reaching 80 kbps while requiring a power of 50 mW for mirror actuation attaining a bit-error-rate of $\approx 10^{-2}$. Xu et al. [2023] used neuromorphic cameras to decode signals up to 6.5 kbps.

In comparison, our proposed system introduces a fundamentally different approach to external light modulation. By using a MHz-scale ultrasound transducer, we overcome the bandwidth limitations of existing modulators, achieving bit error rates of $10^{-4} - 10^{-6}$ with just a single transducer. Unlike LC shutters or DMDs, which require optical enclosures—introducing mechanical and optical integration challenges—our system operates with both the retroreflector and transducer directly submerged in water, simplifying deployment and improving robustness.

2.3 Acousto-Optic Light Sculpting and Beam Steering

Acousto-optic devices—such as deflectors and intensity modulators—steer light using the acousto-optic effect and Bragg diffraction [Jeong et al. 2022; Tsai 2013]. A sound wave propagating through a crystal (e.g., quartz) induces a periodic phase grating, causing an incident light beam to deflect at an angle proportional to the acoustic frequency. These devices are widely used in optical scanners and spatial light modulators and have been explored for visible light communication.

However, Bragg-based acousto-optic modulators rely on frequency modulation to steer the beam, limiting their modulation rates to the kHz range—even when using MHz transducers. Consequently, they are orders of magnitude slower than our proposed approach.

Related technologies such as TAG lenses [Cherkashin et al. 2020; Kang et al. 2020] and ultrasonically sculpted virtual optical waveguides [Chamanzar et al. 2019; Duocastella et al. 2020; Karimi et al. 2019; Pediredla et al. 2023b] offer dynamic control over optical focus and beam guidance and are based on Raman–Nath diffraction regime.

Our technique builds on recent advances in MHz-rate beam steering using phase-modulated acoustic fields [Pediredla et al. 2023a; Sirikonda et al. 2025], enabling spatial modulation of light at MHz speeds. We leverage this fast, lens-free beam steering for high-speed underwater optical backscatter communication.

3 Background: Acousto-optic light steering

Sound is a pressure wave that travels by compressing and rarefying the medium. The medium's density and, hence, its refractive index changes by an amount proportional to the additional pressure introduced by sound.

If we place a flat transducer in a medium and apply a sinusoidal voltage through it, the transducer generates a planar ultrasound wave, which induces a spatiotemporally varying refractive index change in the medium given by

$$\Delta n(x, y, z, t) = \Delta n_{\max} \cos(\underbrace{k_s x - \omega_s t}_{\theta}), \tag{1}$$

where $\Delta n_{\max}$ is a constant proportional to the pressure difference (and hence voltage across the transducer) the ultrasound wave introduces (Fig. 2(a)), k_s is the wavenumber, ω_s is the angular frequency of the ultrasound wave, and θ denotes the total phase.

Pediredla et al. [2023a] interpreted the principal region of this refractive index profile (i.e., $\theta \in [-\pi, \pi]$) as a virtual cylindrical GRIN (Gradient Refractive Index) lens as it has inverse quadratic shape. Furthermore, due to the periodic nature of the cosine function, the ultrasound wave generates an array of cylindrical GRIN lenses, where each lenslet has an aperture equal to the wavelength of the ultrasound wave ($\lambda_s = 2\pi/k_s$). As the ultrasound wave propagates with time, the refractive index in Eq. (1) and hence, the lenslet array also travel at the speed of ultrasound ($c_s = \omega_s/k_s$) as shown in Fig. 2(b).

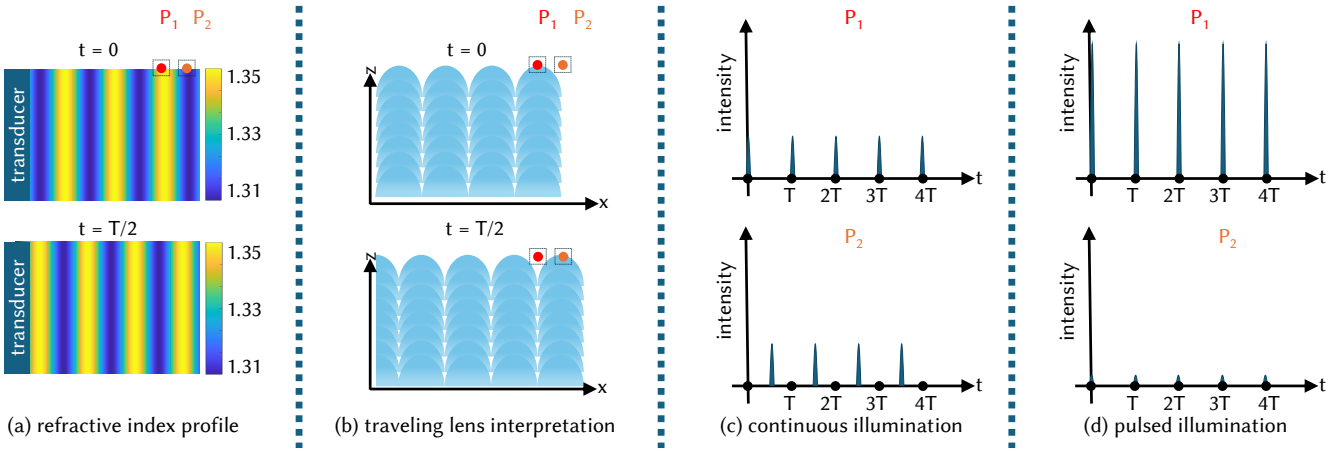

Fig. 2. *Acousto-optic light steering* (a) Similar to Pediredla et al. [2023a], we use a planar transducer to create a sound wave. When a single monotone is played through this transducer, a spatially and temporally varying sinusoidal pressure wave is created in the medium, generating a refractive index change proportional to the pressure. (b) The net effect can be modeled as a series of cylindrical gradient refractive index (GRIN) lenses with an aperture equal to the ultrasound wavelength that travel at the speed of sound in the medium (1.5 km/s for water). We show the location of the lenses at two time instants, $t = 0$ and $t = T/2$. We also show two points (P_1) and (P_2) on the focal plane of these GRIN lenses. (c) If the light source is continuous, the temporal intensity at any point on the focal plane will be a series of periodic impulses with the same frequency as ultrasound and different phase shift. (d) In our hardware implementation, to increase signal-to-noise ratio, we used a pulsed laser synchronized with the ultrasound frequency, starting at time $t = 0$. When the detector is positioned at the focal point (P_1), it records high-intensity, periodic illumination pulses. Conversely, if the detector is placed at a defocused point (P_2), ideally it doesn't detect any light. However, due to imperfections, it detects weak illumination pulses.

Assuming that the virtual cylindrical lenslet array is free of aberrations and the illumination is a collimated light beam. The light intensity at the focal plane $z = f$ will be a series of impulses traveling in space, given by

$$I(x, y, z = f, t) = P \sum_k \delta(x - k\lambda_s - c_s t), \tag{2}$$

where δ is the standard Dirac delta function and P is proportional to laser's optical power. In practice, the laser beam has a spatially extent and P will vary spatially; the GRIN lenslet has aberrations and diffraction blur and therefore the Dirac delta function will become a spatio-temporal blur kernel. However, for simplicity in explanation, we will ignore these effects and will refer to them when they are important.

A point sensor placed at any location on the focal plane will observe a series of impulses over time. In Fig. 2(c), we visualize these impulses for two points, P_1 and P_2, which are separated by a distance equal to half of the ultrasound wavelength. This separation causes a phase shift of π between the impulse trains.

In our system, we use a pulsed laser operating at the same frequency as ultrasound. A pulsed laser emits ultrashort laser pulses (nanoseconds to picoseconds) with duty cycle $\approx 10^{-2}$ localizing the light energy to an extremely short time period increasing signal-to-noise (SNR) ratio. In that case, we can assume that we are illuminating only when the lenslet array is at a specific position and not illuminating for all other positions. Correspondingly, only points on the focal plane at the optical centers of these lenses observe impulse trains, and all other points receive no light Fig. 2(d). Mathematically,

$$I(x, y, z = f, t) = \sum_k \delta(x - k\lambda_s)\delta(t \bmod T), \tag{3}$$

where T denotes the time period of sound wave ($T = 2\pi/\omega_s$).

4 Proposed communication technique

As shown in Fig. 1, we assume that a remote asset is navigating (e.g., surveying, constructing, cleaning) underwater at sea and communicating with a central base station that is coordinating it. The base station could be tethered to the ship, as commonly done in marine robotics operations [Choi and Yuh 2016], and has significantly more resources to track and send data to the mobile assets

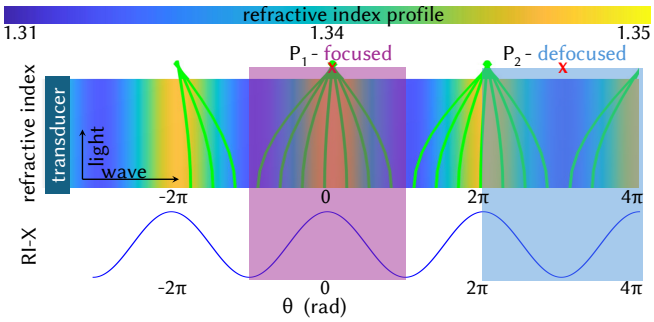

Fig. 3. The figure illustrates how light rays, traveling parallel to a gradient refractive index profile, undergo focusing and defocusing. When $\theta \in [-\pi, \pi]$ (highlighted in purple), the light rays converge towards the center as the refractive index has inverse-quadratic-like shape. When $\theta \in [0, 2\pi]$ or $\theta \in [2\pi, 4\pi]$ (highlighted in blue), the light rays diverge away from the center as the refractive index in this region has quadratic looking shape. We use this understanding to design waveforms that either focus light to encode bit 1 (P_1) or defocus light to encode bit 0 (P_2).

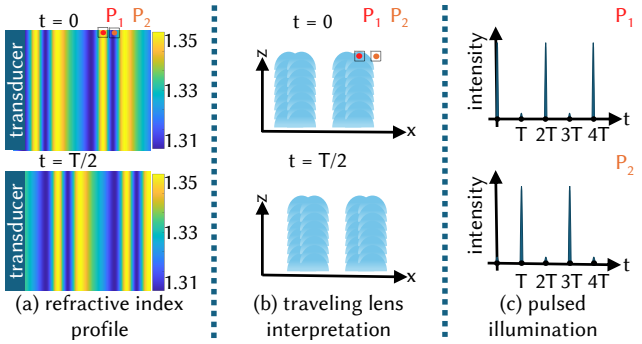

Fig. 4. *Proposed light steering to encode the bit stream optically.* (a) Instead of using a pure sinusoid, we phase-modulate the sound wave to encode the bit-stream. (b) This phase modulation results in cylindrical GRIN lenses at non-uniform distances. (c) We use pulsed illumination similar to Fig. 2(d). Instead of receiving a series of pulses, we either receive a focused, high-intensity laser pulse (bit 1) or low-intensity light pulse (bit 0) based on the phase modulation. The point P_2, located at half a wavelength distance from P_1, receives the inverted bit stream and could be used to improve the robustness.

through traditional communication techniques, including pulsing the lasers. The base station must include at least one high-speed photodetector (i.e., with high temporal bandwidth), a digitizer to convert the detector's output to digital signals, and a pulsed laser source that is co-located with the photodetector. The remote asset meanwhile has a retroreflector to reflect the laser beam towards the base station and a transducer to modulate the laser beam to either have high intensity at the detector to encode *bit* 1 or low intensity at the detector to encode *bit* 0.

Our key observation, which extends Pediredla et al. [2023a]'s interpretation, is to notice that while all the rays interacting with $\theta \in [-\pi, \pi]$ in Eq. (1) converge towards $\theta = 0$, all rays interacting with $\theta \in [0, 2\pi]$ region are diverging as shown in Fig. 3. Therefore, we have to design the transducer voltage waveform to have inverse quadratic waveform to focus light (*bit* 1) and quadratic waveform to defocus light (*bit* 0). However, the transducer also requires a smooth waveform that has as high contrast as possible to generate large refractive index gradient. To achieve these goals, we phase modulate the sinusoidal input to transducer, similar to Pediredla et al. [2023a] and ensure that voltage is as high as possible to encode *bit* 1 and as low as possible to encode *bit* 0. While this doesn't necessarily ensure that the lobe around the bits still has quadratic or inverse quadratic-like behavior, we develop bit redundancy to ensure this.

The refractive index profile with phase modulation will be:

$$\Delta n(x, y, z, t) = \Delta n_{\max} \cos(k_s x - \omega_s t + \phi(t)), \tag{4}$$

where $\phi(t)$ is the phase modulation. Fig. 4(a, b) show the spatially varying refractive index profile at two time instances and the corresponding GRIN lenses.

Illuminating these GRIN lenslet arrays with periodic laser pulses, and ignoring diffraction blur and aberrations, we measure a spatio-temporal pulse train at the focal plane $z = f$:

$$I(x, y, z = f, t) = \delta(x - c_s t + \phi(t)/k_s \bmod \lambda_s)\delta(t \bmod T). \tag{5}$$

The location of the focal plane f is inversely proportional to the voltage across the transducer, which is calibrated to ensure that the photodetector is located on the focal plane of the virtual lenslet array. Similarly, the initial phase offset of the transducer is calibrated to ensure that the photodetector is located at $x = 0$. The measurement at the detector would be

$$\begin{aligned} I(t) &= \delta(c_s t - \phi(t)/k_s \bmod \lambda_s)\delta(t \bmod T); \\ \therefore I(kT) &= \delta(\phi(kT)/k_s \bmod \lambda_s), \end{aligned} \tag{6}$$

for $k = 0, 1, 2, \cdots, K-1$, i.e., K laser pulses. In practice, due to aberrations and diffraction blur, we will not get sharp Diracs but observe a spatio-temporal blur.

Given a binary bitstream $b[k]$ that the remote asset intends to transmit, we require $I(t) = \sum_k b[k]\delta(t - kT)$. For each bit $b[k] \in \{0, 1\}$, we achieve this by either letting the light focus on the detector (*bit* 1), by setting $\phi(kT) = 0$, or by defocusing, i.e., focusing the light as far away as possible from the detector (*bit* 0) by setting $\phi(kT) = k_s\lambda_s/2 = \pi$. Theoretically, if the aberrations and diffraction blur are absent, to achieve $b[k] = 0$, $\phi(kT)$ could be any value other than an integral multiple of 2π.

To compute continuous $\phi(t)$ from these discrete time samples (at $t = kT$), we use cubic B-spline interpolation [Unser 1999] with periodic boundary conditions. We empirically found spline interpolation to be better than sinc or linear interpolation.

Bit Decoding: The photodetector at the base station measures the intensity of retroreflected light from the remote asset. The digitizer samples this analog signal and converts it into digital data, which is then thresholded to recover the transmitted bitstream.

4.1 Voltage and Offset Calibration

As mentioned earlier, the voltage applied to the transducer controls the refractive index gradient, thereby adjusting the focusing strength of the virtual cylindrical lens array. To focus light onto the base station, we can precompute voltage settings for a range of receiver distances and use these during operation.

Our system has an extremely large depth-of-field due to the small aperture size of each virtual cylindrical lens—approximately equal to the wavelength of sound in water. For example, with a 2 MHz transducer and the speed of sound at room temperature $c_s = 1.5$ km/s, the acoustic wavelength (and thus the aperture size) is about 0.75 mm. At a target distance of 1 m, this results in a depth-of-field of approximately 0.67 m, enabling robust focusing over a wide range without frequent recalibration.

Empirically, we changed the voltage values till the light focused on the detector. We didn't notice any significant difference in the system for a large voltage range (detailed analysis in Sec. 6.1.1).

To ensure that the photodetector is at the origin (Eq. (6)), we transmit all ones and sweep the phase till we observe the highest intensity at the photodetector.

4.2 3-bit Redundancy

For the ultrasonic waveform to encode binary bit stream, we wanted the waveform to be smooth, have highest intensity while transmitting *bit* 1, lowest intensity while transmitting *bit* 0 and lobes around

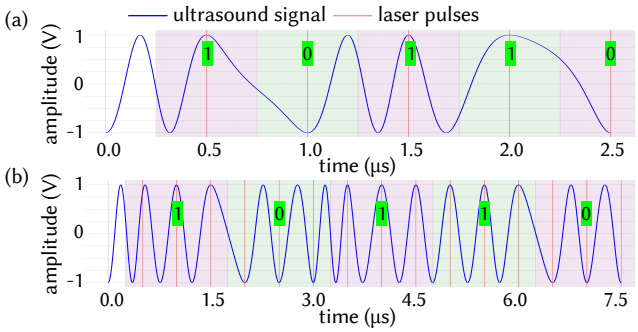

Fig. 5. *Synthesized Waveforms.* (a) We show the intended signal `[1 0 1 1 0]` to be sent through the channel. Red lines indicate laser firing times. The waveform is constructed so that wave peaks (bit 1) and valleys (bit `0`) align with laser pulses. The region around the bits no longer has quadratic or inverse-quadratic like shape. (b) The 3-bit redundant signal ensures the central bit in each triplet has the expected shape.

the *bit* 1 transmission to be inverse quadratic shaped and *bit* `0` to be quadratic shaped.

In Fig. 5(a), we show the synthesized waveform with phase modulation. We could observe that the lobes around the bits are skewed and are affected by adjacent bit values. To mitigate this problem, we applied a 3-bit redundancy, repeating each bit three times. This repetition isolates the center bit in each triplet from adjacent transitions, improving the lobe around the transmitted bits, enhancing communication reliability.

Fig. 5 demonstrates this encoding strategy. In this case, we transform the sequence `[1 0 1 1 0]` into `[1 1 1 0 0 0 1 1 1 1 1 0 0 0]` before transmission.

This 3-bit repetition reduces the effective data rate to one-third, lowering the bitrate to approximately 0.66 Mbps ($\frac{2\,\text{MHz}}{3} = 0.66\,\text{MHz}$). Despite this reduction, the system still operates 60× faster than existing optical backscatter communication systems.

4.3 Efficient Waveform Synthesis

Exact cubic B-spline interpolation (Box 2 in Unser [1999]) requires access to the entire bitstream (i.e., one transmission packet) to compute the waveform. This increases overall latency and also the computational cost.

To address this challenge, we employ an approximate yet computationally efficient strategy based on a look-up table (LUT). Since each cubic B-spline interpolation kernel influences at most three bits, we precompute the waveform segments corresponding to both *bit* `0` and *bit* 1, considering all possible combinations of the immediately preceding and succeeding bits. This results in an LUT of size 8. During waveform synthesis, we determine the appropriate LUT entry by examining the bits immediately adjacent to each target bit in the bitstream. The corresponding precomputed waveform segment is then directly used for synthesis. This approach substantially reduces encoding latency by eliminating the need to process the entire bitstream, while preserving smooth transitions in the generated waveform.

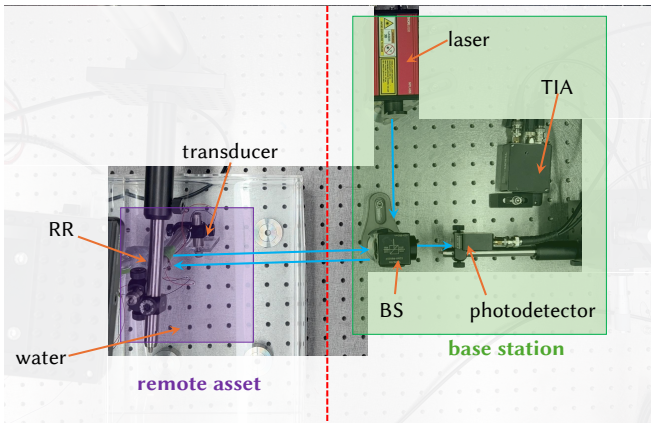

Fig. 6. *Hardware Prototype*: We construct a base station by colocating a pulsed laser and a photodetector using a beamsplitter. The remote asset, submerged in a water tank without any optical enclosures, consists of a total internal reflection (TIR)-based retroreflector and an ultrasonic transducer. The only waterproofing requirement is for the back surface of the retroreflector, which must remain sealed to maintain total internal reflection. The laser beam emitted from the base station is retroreflected by the remote asset. The ultrasonic transducer modulates this reflected light using the acousto-optic effect to encode a binary bitstream. The base station's high-speed photodetector captures the modulated retroreflected light, which is then amplified via a transimpedance amplifier (TIA) and subsequently decoded to recover the transmitted binary information.

We empirically compared the spline-based and LUT-based implementations and found that the generated waveforms are nearly identical, with a maximum deviation of only 3.45×10^{-7} over a one second signal ($1\,\text{s} \times 0.66\,\text{Mbps} = 0.66\,\text{Mbit}$). The spline interpolation takes approximately 25 min on a single CPU core and 100 s on a 32-core machine. In contrast, the LUT-based implementation achieves near real-time performance, completing in approximately 1.36 s on a single core, and as fast as 0.08 s with vectorized implementation. Depending on the available resources, LUT-based pipelines can be readily deployed for efficient waveform generation. Additionally, the LUT-based approach yields highly compressible signals. For a 1 s waveform, we observed reductions of nearly two orders of magnitude: repeated patterns map to identical stored values rather than slightly differing floating-point samples, reducing redundancy and enabling compact storage—especially when only a small set of transitions (e.g., 3-bit) needs to be encoded.

5 Hardware Prototype

In this section, we describe the hardware prototype we built to validate and characterize the proposed backscatter communication technique. The hardware prototype consists of two main components: (1) a base station and (2) a remote asset. Fig. 6 illustrates the optical path and the physical arrangement of these components within the system.

Base Station: The base station is equipped with a pulsed laser (Thorlabs NPL45B) that emits a beam directed through a 50:50 beamsplitter (Thorlabs BS004). The beamsplitter divides the beam into two paths; we utilize the path that enters the water medium and occlude

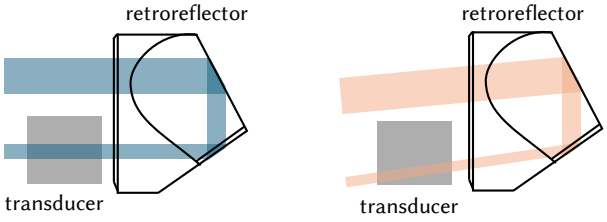

Fig. 7. *Retroreflective design.* The side view shows the transducer near a retroreflector mirror so light interacts with the acoustic wave only once.

the other using a beam block. A high-speed photodetector (Thorlabs DET25A), also located at the base station, captures the retroreflected light from the remote asset. The detected signal is amplified using a transimpedance amplifier (Thorlabs TIA60) and digitized via a PC-based oscilloscope (Picoscope 3418E). The resulting digital signal is then thresholded to decode the transmitted bitstream.

Remote Asset: The remote asset comprises a 2 MHz ultrasonic transducer (APC International, model #1976) paired with a total internal reflection (TIR)-based retroreflector (Thorlabs PS975M-A-TIR). Since efficient TIR requires a glass-to-air interface at the rear surface, we hermetically seal the back of the retroreflector to preserve its reflective efficiency. The assembled system is submerged in an acrylic tank filled with water.

To minimize secondary interactions between the acoustic reflections and the optical beam, we orient the transducer at an oblique angle with respect to the tank walls. Furthermore, to ensure that only one of the incident or reflected optical paths interacts with the acoustic field, we position the transducer near one of the retroreflector's internal mirrors, as illustrated in Fig. 7.

To encode the bitstream, we first convert it into a voltage waveform using the phase modulation scheme described in Sec. 4. This waveform is synthesized using an arbitrary waveform generator (Spectrum Instrumentation M2p.6531-x4) and then amplified to the required voltage level, as detailed in Sec. 4.1. The amplified signal drives the transducer, which generates a modulated acoustic field in the water. This field induces acousto-optic interactions that deflect the light rays, thereby encoding the bitstream in the retroreflected optical signal.

Effect of 3-bit redundancy: Using the prototype, we first evaluated the impact of 3-bit redundancy (Sec. 4.2). In this scheme, each bit is transmitted as three consecutive pulses, and the central pulse is used for detection. In Fig. 8, we compare the photodetector output with and without the use of 3-bit redundancy. While this redundancy reduces the effective bitrate by a factor of three, it significantly enhances the contrast between *bit* 1 and *bit* 0, thereby improving the system's robustness to both threshold selection and noise.

6 Experimental Evaluation

In this section, we first evaluate the overall performance of the prototype by assessing its capability to transmit various data types, its energy consumption, and its effective communication range. We

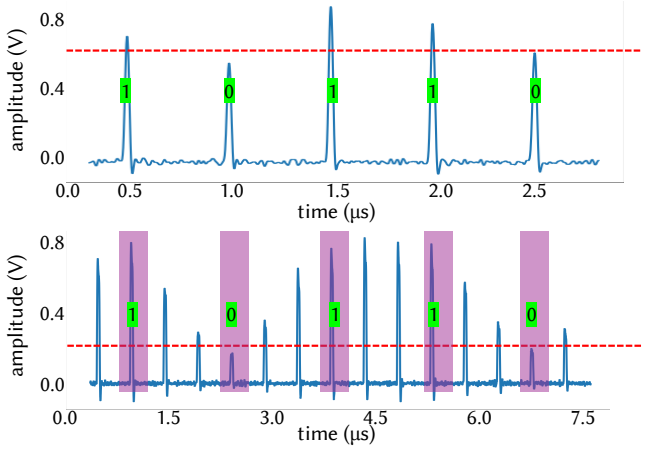

Fig. 8. *Effect of 3-bit redundancy.* We visualize the photodetector output both with and without the application of 3-bit redundancy. (top) Without redundancy, the contrast between *bit* 1 and *bit* 0 is relatively low ($\frac{0.7}{0.6} \approx 1.167$), making the signal more susceptible to noise and resulting in a higher bit error rate. (bottom)With redundancy, where the central pulse is used for decoding, the contrast improves significantly ($\approx \frac{0.8}{0.2} \equiv 4.0$), leading to increased robustness against noise and a lower likelihood of bit errors.

then characterize the system's robustness under adverse environmental conditions, including water turbulence, ambient illumination, and acoustic interference.

Throughout this section, we evaluate the bit error rate (BER) by transmitting 20 packets per experiment. Each packet contains 0.66 Mbit of data, corresponding to 2 Mbit or 1 s of raw data with 3-bit redundancy applied.

6.0.1 Testing with Various Data Modalities. We evaluate the system's ability to handle diverse data formats by transmitting audio (WAV), images (JPEG), and video (MP4 and TS). For these tests, we position the remote asset 2.5 m away from the base station and transmit all data at a constant rate of 0.66 Mbps.

Each data type presents unique challenges in terms of signal integrity and bitstream resilience, enabling a comprehensive assessment of transmission fidelity. For the audio test, we transmit a spoken phrase—"Hello SIGGRAPH Asia!"—in `WAV` format. Fig. 9 displays spectrograms of the transmitted and received signals along with their pitch contours, which show near-perfect alignment. (The supplement includes audio playback for both.)

To emulate visual sensing tasks in underwater environments, we transmit pre-captured underwater images. Due to the inherent quality degradation in such images caused by underwater conditions, we augment the dataset with AI-generated underwater images, all encoded in JPEG format. JPEG's high sensitivity to bitstream corruption makes it a strong benchmark for evaluating data integrity. Additionally, we transmit video files in MP4 and TS formats to assess the system's performance under both compressed and continuous-stream data transmission scenarios.

All transmissions are successfully reconstructed with low BER. Fig. 10 shows side-by-side comparisons of transmitted and received images, while Fig. 11 presents representative frames from the video

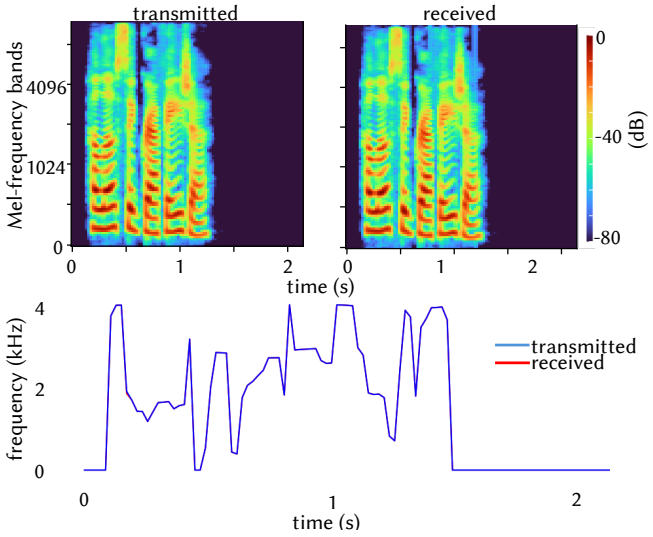

Fig. 9. The figure displays the Mel-spectrogram of the transmitted audio signal (left) and the received signal (right). The pitch contour below illustrates the accuracy in preserving the signal's pitch. The transmitted audio sample contains the phrase "Hello SIGGRAPH Asia!". We repeated this experiment multiple times and are showcasing a single instance where the BER is non-zero. Despite this, the pitch contour exactly matches the signal.

Fig. 10. The figure shows JPEG-encoded images transmitted using our underwater communication system. Images of sizes 0.8 Mbit to 10.4 Mbit of data. We overlay the Peak Signal-to-Noise Ratio (PSNR) at the right top and Mean Squared Error (MSE) at the left bottom of each image to quantify reconstruction quality. Original and received versions are shown in the top and bottom rows, with full-resolution versions included in the supplement.

sequences. Some image transmissions achieve nearly 100 % reconstruction accuracy, while others exhibit minor visual degradation with BERs on the order of $\approx 1.0 \times 10^{-4}$. The PSNR and the MSE metrics of the transmissions are reported in the insets of the Fig. 10 and Fig. 11. Across all formats, the average BER remains low at $\approx 1.0 \times 10^{-4}$, despite the absence of error-correcting codes.

6.1 Overall Performance

These results underscore the system's robustness across a wide range of media formats. Its ability to reliably transmit high-fidelity audio, images, and video streams at high speed sets it apart from

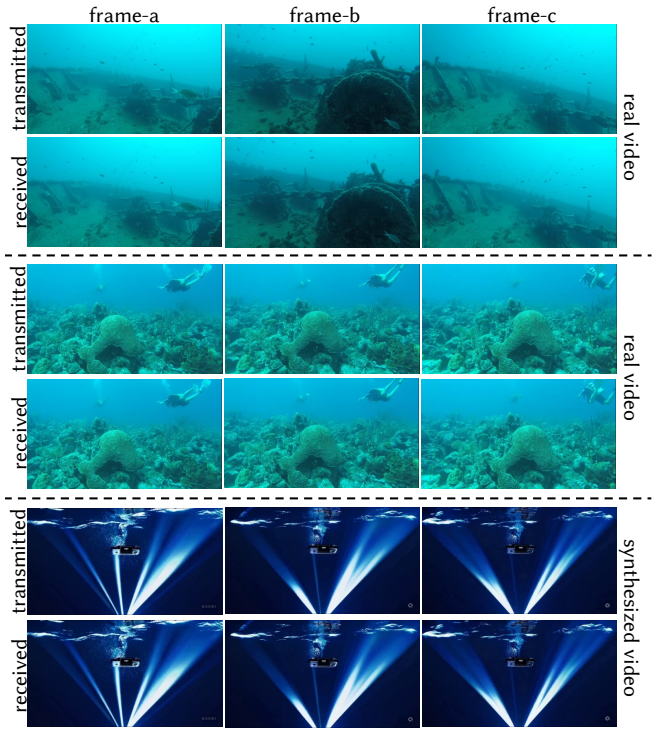

Fig. 11. The figure shows sampled frames from 3 videos. In each segment, the top row displays original frames from the video, while the bottom row shows the corresponding frames at the same timestamps after transmission. The first two videos are real underwater recordings, while the third video was synthetically generated using SORA (a ChatGPT-based AI tool).

existing optical backscatter systems and conventional underwater acoustic transmission systems, which are typically constrained to text-based communication due to limited bandwidth. Our system achieves data rates over two orders of magnitude higher (> 100×) than these traditional approaches, thereby enabling rich, multimedia-capable underwater sensing and communication.

6.1.1 Energy Consumption for Transmission. As discussed in Sec. 4 and Sec. 5, we apply voltage across the transducer to focus the illumination beam. This voltage directly influences the prototype's power consumption.

As described in Eq. (1), effective lens sculpting requires the transducer to operate within an optimal voltage range. The strength of the acoustic lensing effect increases with applied voltage [Pediredla et al. 2023a]. At low voltages, the acoustic field is insufficient to form a well-defined lens, resulting in weak or unfocused light propagation. Conversely, at high voltages, the lens focuses the light in front of the detector, leading to blurred waveforms and degraded bitstream integrity. In both cases, deviations from the optimal voltage range impair the quality of data transmission.

To characterize this behavior, we experimentally vary the transducer voltage and record the resulting BER. Fig. 12 plots the BER observed at each voltage level. The results show that the system maintains reliable performance for a large voltage range of 8 V to

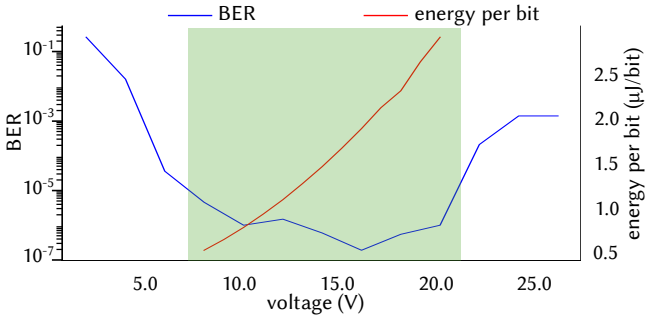

Fig. 12. The BER remains below 1×10^{-4} for a wide operational voltage range of 8 V to 20 V, ensuring reliable communication. The BER values are plotted on the left y-axis in a **logarithmic scale**, while the corresponding energy per bit is shown on the right y-axis.

Table 2. **BER Across One-Way Transmission Distances.** The system maintains a consistently low BER even at longer distances, demonstrating robust communication performance.

Distance (m)	**BER ($\times 10^{-7}$)**
1.5	19
2.7	27
3.86	55
5.0	1.5

20 V. Notably, the system achieves a BER on the order of 10^{-5} at 8 V, where energy consumption per bit is also quite low. These findings demonstrate that the system operates efficiently across a broad voltage range, supporting low-power, high-fidelity communication. The minimum energy consumed by our system is ≈0.226 μJ/bit.

6.1.2 Tested Transmission Distance. The experiments presented in the previous sections demonstrate that the system can reliably transmit data at 0.66 Mbps. To assess its performance over longer distances and under more realistic conditions, we conducted preliminary field tests in a water body. However, environmental factors such as buoyancy, turbulence, and water currents demand a mechanically stable and robust base station—a non-trivial engineering challenge [Shen et al. 2021] that falls outside the scope of this work.

To circumvent this constraint, we developed a benchtop setup that emulates long-distance transmission using a folded optical path, as illustrated in Fig. 13. This experimental strategy aligns with methodologies adopted in prior optical communication research, such as Wu et al. [2017].

We constructed the folded-path setup using two 5 cm diameter broadband mirrors (Thorlabs BB2E02), mounted in parallel on precision kinematic mounts (Thorlabs KM200). These mirrors, placed inside a 0.75 m glass tank, reflect the laser beam repeatedly along the tank's length before it reaches the retroreflector.

Fig. 13(a) shows the full experimental layout used for long-range, one-way transmission tests. As illustrated in Fig. 13(b), the laser beam follows a folded trajectory, achieving an effective one-way distance of up to 5 m. By adjusting the kinematic mounts, we tune

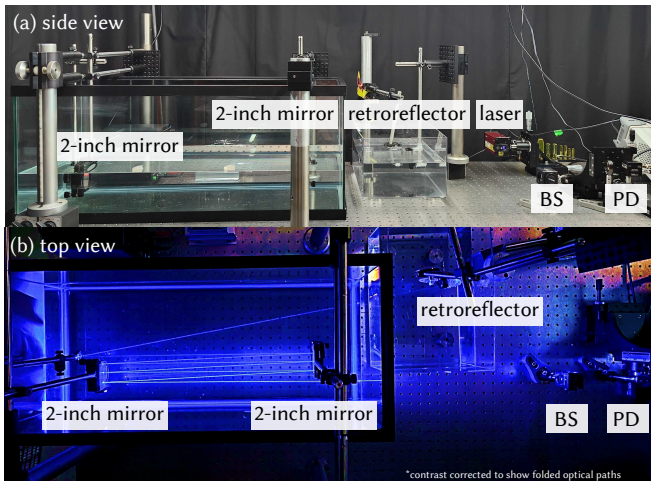

Fig. 13. (a) *Experimental Setup for Long-Distance Laser Transmission Using Parallel Mirrors.* Two parallel-mounted mirrors are suspended inside a 30-inch glass tank to reflect the laser beam multiple times along the tank's length before directing it toward the retroreflector. (b) *Beam Path in Long-Distance Transmission Experiment.* The laser beam reflects three times off each of two parallel mirrors 24 inches apart, creating a folded optical path. A small angled mirror then redirects the beam toward the retroreflector for signal modulation and return.

the transmission distance from a minimum of 1.5 m–where the beam reflects off a single mirror point–to a maximum of 5 m.

This configuration enables controlled testing of the system across multiple effective transmission distances. At all tested distances, the system consistently maintains a BER at or below 5.5×10^{-6}, confirming reliable performance over extended ranges. We summarize the BER results in Tab. 2.

While 5 m was the maximum transmission distance achievable in our laboratory setup, we conducted additional experiments to investigate the system's practical range limits. Specifically, we introduced scattering media into the optical path to emulate the attenuation effect of longer-distance propagation. This allowed us to estimate the theoretical maximum transmission distance of the system.

6.1.3 Theoretical Transmission Distance Limit. To understand the theoretical transmission distance limit of our system as well as understand its performance in the presence of scattering particles, we conducted a series of experiments by incrementally adding milk powder to 7.5 L of clean water. As scattering increases, we measured both the corresponding reduction in received light intensity at the photodetector as well as the BER. We continued the experiment until the received light fell below the photodetector's detection threshold.

The relationship between laser intensity (I_{source}), received light intensity (I_{dest}), optical efficiency (f_l), diffuse attenuation coefficient (k_d) and distance (d) is given by Smith and Baker [1981],

$$I_{\text{dest}} = I_{\text{source}} \cdot f_l \cdot e^{-d \cdot k_d}, \tag{7}$$

which is the also standard Beer-Lambert law. The one-way optical distance the beam travels in the water is 0.45 m. We use this to compute k_d for different scattering levels, as shown in Tab. 3. For

Table 3. BER under increasing scattering. RLI: Received Light Intensity, EqD_s: equivalent distance in clear sea water derived from the seawater attenuation coefficient $k_d = 0.017/\text{m}$, EqD_c: equivalent distance in coastal water from Baltic sea ($k_d = 0.24/\text{m}$).

RLI (mW)	EqD_s (m)	EqD_c (m)	k_d (1/m)	Milk (mg)	BER $\times 10^{-6}$
3.600	0.450	0.05	0.018	0	0.50
3.300	5.300	0.42	0.211	200	2.50
3.100	8.700	0.68	0.350	400	12.0
2.900	12.40	0.95	0.490	600	12.0
2.600	18.30	1.41	0.741	800	54.0
2.200	27.20	2.10	1.110	1000	140.0
1.700	42.10	3.18	1.680	1200	170.0
1.200	61.40	4.63	2.450	1600	410.0
0.700	91.40	6.88	3.650	2000	560.0

all these scattering levels, the system maintained reliable communication ($\leq 1 \times 10^{-3}$ BER) up to a diffuse attenuation coefficient of $k_d = 3.65/\text{m}$. For reference, k_d for clean sea water is $0.017/\text{m}$ [Smith and Baker 1981] and coastal waters in Baltic Sea are $0.24/\text{m}$ [Mobley 2010].

In Tab. 3, using Eq. (7), we computed the equivalent distance if the water is not mixed with milk particles but instead is pure sea water (2nd column) or coastal water (3rd column). Based on these values, we can conclude that our system can theoretically transmit to around 91.40 m in sea water and 6.8 m in coastal murky waters. It is important to note that these estimates are based on a laser with an output power of 5.4 mW. Higher-power lasers could enable longer transmission distances; however, the gains are subject to diminishing returns, as governed by the logarithmic relationship in Eq. (7).

6.2 Effect of External Environmental Factors

Beyond the overall performance demonstrated in Sec. 6.0.1, we evaluate the system under challenging environmental conditions that may degrade transmission quality. Specifically, we test its robustness to three key factors: water turbulence, external illumination, and acoustic interference.

6.2.1 Water Turbulence. To simulate turbulence, we introduce controlled water currents into the communication channel using a voltage-controlled rotating wheel with a diameter of 6.2 cm, as illustrated in Fig. 14(a). The wheel generates surface waves within the tank, emulating dynamic underwater flow conditions. We approximate the current speed as the tangential velocity at the wheel's edge:

$$v = r \times \omega, \tag{8}$$

where r is the wheel's radius and ω is its angular velocity. Actual flow velocities may exceed this estimate due to reflected currents within the small tank.

Fig. 14 presents the effect of water turbulence on bit error rate (BER). At low wheel speeds, surface motion minimally impacts transmission. However, as the wheel speed increases, interactions between the induced currents and the tank walls generate observable turbulence and bubbles, which interfere with the backscattered optical beam, as shown in Fig. 14(b). Despite these disturbances, the system maintains a low BER of 2×10^{-4}.

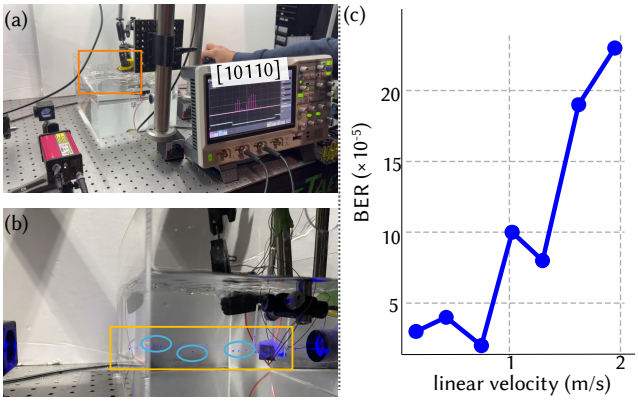

Fig. 14. (a) The figure illustrates water currents introduced into the communication system using a voltage-controlled wheel with a diameter of 6.2 cm. The oscilloscope displays the received signal `[1 0 1 1 0]`, where each peak corresponds to transmitted data with its 3-bit redundancy, despite the presence of water currents. (b) The image captures bubbles generated by these currents as they interfere with the backscattered beam transmitting the data. (c) The BER, plotted against linear currents, demonstrates the system's performance. Even at higher currents of 2 m/s, the BER remains within an acceptable range, indicating the system's resilience to flow-induced disturbances despite the presence of bubbles in the communication beam's path.

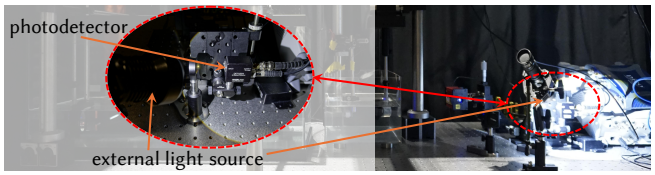

Fig. 15. The figure illustrates the physical arrangement of the high-lumens torch pointing towards the photodetector used for studying the effect of external illumination.

For context, typical underwater current speeds range from 0.01 m/s to 0.2 m/s [Damuth and Olson 2001], significantly lower than the 2 m/s condition tested here. These results confirm the robustness of our system under realistic and even exaggerated flow conditions.

6.2.2 External Illumination. Since the system relies on visible light communication, external illumination sources—such as ambient lighting or directed beams—can interfere with the photodetector and degrade signal quality. To assess the system's susceptibility to such interference, we conducted two controlled experiments: (1) we directed a high-intensity torch emitting 12 000 lx at the photodetector, and (2) we exposed the entire setup to natural sunlight, replacing the dark-room conditions typically used during testing.

High Lumen Torch: In the first experiment, we directed a bright mounted torch at the photodetector, resulting in an ambient light level of approximately 12 000 lx at the detector (Fig. 15(a)). This high

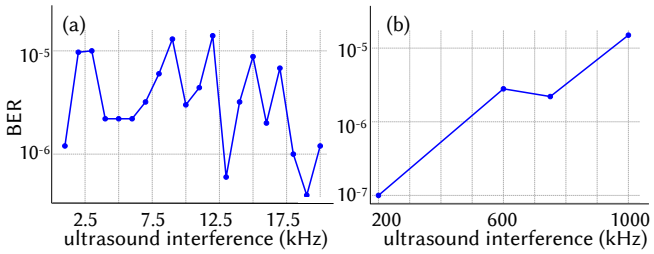

Fig. 16. (a) The graph shows the observed BER when external sonic frequencies are applied in the transmissive media which can interact with the system's ultrasound. (b) The graph shows effect of introduction of ultrasonic frequencies to the transmission.

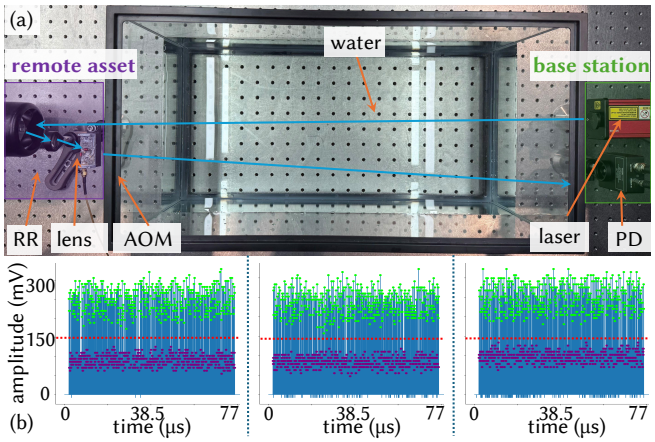

Fig. 17. *AOM Experimental Setup:* (a) Figure shows the experimental configuration for Raman–Nath diffraction using an Acousto-Optic Modulator (AOM). The retroreflected laser beam is focused onto a localized region of the AOM crystal, which performs phase modulation necessary for communication. The modulated beam is then detected by a photodetector at the base station. The blue arrows show the light path and the components like retroreflector (RR), lens, AOM, laser, photodetector (PD) are marked accordingly. (b) We visualize the photodetector outputs for the AOM operating at 39 MHz, with communication occurring at 13 Mbps. Each signal contains 1000 bits, and the bits (0 and 1) are separated by a threshold line at 150 mV. We show three representative output traces demonstrating consistent signal clarity.

illumination introduced a DC offset of about 60 mV in the received signal. Despite this interference, the system maintained reliable performance with a measured BER of 4.7×10^{-5}.

Sunlight: In the second experiment, we fully opened the blinds to allow maximum natural light into the room, simulating ambient illumination. Under these conditions, the measured light level at the detector reached approximately 300 lx, resulting in a smaller offset of about 5 mV in the received signal. The system achieved a BER of 2.0×10^{-5}, confirming robust operation even in the presence of natural lighting.

Note that, we have not used a bandpass filter to remove the ambient light. Adding such a filter on the photodetector will make our system robust to even strong sunlight (120 000 lx) conditions.

6.2.3 External Acoustic Interference. We next evaluate the impact of external sonic and ultrasonic frequencies that may interfere with optical transmission. To characterize potential acoustic interference, we tested the system across two frequency ranges: 2.5 kHz to 20 kHz, representing common sonic disturbances, and 0.2 MHz to 1 MHz, covering typical ultrasonic sources. These ranges align with operational bands commonly used in underwater systems for communication, sonar imaging, and structural inspection.

For testing, we placed the external acoustic transducer next to the main 2 MHz transducer to maximize the interference. The resulting BERs are shown in Fig. 16. Across all tested frequencies, the system maintained a consistently low BER on the order of 1×10^{-5}, demonstrating strong resilience to acoustic interference.

This robustness is primarily due to the large frequency gap between the external disturbances and the system's driving frequency. Since most external acoustic sources operate at significantly lower frequencies than the modulated ultrasound used in the prototype, their influence on the refractive field–and thus on the optical beam–remains minimal.

7 Conclusions and future work

We have designed and implemented a laboratory prototype for robust, high-speed underwater optical backscatter communication, utilizing acousto-optic beam steering. The system achieves data rates of up to 0.66 Mbps using a 2 MHz acoustic transducer. Through extensive emulated experimentation, we demonstrated that the research prototype can reliably transmit large and complex files, while maintaining robustness against underwater currents, ambient illumination, and acoustic interference. *While these results are encouraging, translating the prototype beyond the laboratory raises practical challenges; we first summarize these limitations, then outline a roadmap to address them.*

Limitations. Preliminary experiments in a water body underscored the gap between laboratory robustness and deployment. While the *communication method* itself is tolerant to flow-induced perturbations, the *field enclosures and mounts* were susceptible to hydrodynamic loads: water currents induced platform motion and optical misalignment, consistent with prior reports on vehicle stability in flow and field operations [Phillips et al. 2023; Yoon et al. 2024]. Corrosion further degraded fasteners and opto-mechanical interfaces over time, aligning with established observations and mitigation practices for marine systems [Odeyemi and Alaba 2025]. These issues point to the need for watertight, neutrally buoyant, and hydrodynamically stable housings and materials before open-water deployment [Ma et al. 2021]. For context, pool-based underwater optical wireless communication studies commonly emulate flow/turbulence to characterize link robustness [Vali et al. 2018]. Taken together, these lessons provide concrete engineering targets and a clear path toward robust open-water trials.

Roadmap for future work. Guided by the above limitations, we next describe concrete directions to increase performance and move toward field-ready operation.

(1) Solid prototype with higher bit rate. While our primary results utilize a 2 MHz transducer, a natural question arises: how

does our system compare to commercially available acousto-optic modulators (AOMs), which typically employ higher-frequency transducers? To address this, we first review the operating principles of commercial AOMs.

A single-frequency acoustic wave propagating through an AOM induces a refractive index modulation, forming a periodic structure analogous to that described in Eq. (1). Commercial AOMs, including intensity modulators, treat this periodic modulation as a diffraction grating. When a light beam with a diameter much larger than the acoustic wavelength interacts with this grating—within the Bragg diffraction regime—it generates multiple diffracted orders. Steering the light requires altering the sound wave's frequency, a process inherently slower than phase modulation, limiting commercial AOMs (even those operating in the MHz range) to modulation speeds in the kHz range.

In contrast, Pediredla et al. [2023a], Sirikonda et al. [2025], Duocastella et al. [2020] operate in the Raman-Nath regime by illuminating only a few acoustic wavelengths and relying on phase modulation which is faster. Interestingly, tightly focusing the input beam on a small region of a commercial AOM crystal and subsequently expanding the output can transition the system from Bragg to Raman–Nath diffraction, producing the characteristic line-based diffraction pattern instead of discrete diffraction spots. An alternative—though less efficient—approach is to illuminate a standard AOM and expand one of its diffracted orders.

To experimentally evaluate this hypothesis, we employed a 39 MHz commercial AOM for optical backscatter experiments. As shown in Fig. 17, we achieved a data rate of 13 Mbps. Due to the cost of commercial AOMs, we avoided submerging the device in water. Instead, we introduced a large water volume between the base station and the remote asset to approximate underwater conditions. These commercial AOMs are highly optimized, featuring impedance-matched circuitry and low energy consumption (6 nJ/bit), while maintaining high optical contrast between *bit* `0` and *bit* 1, as seen in Fig. 17(b).

Due to hardware constraints, we were unable to conduct more extensive evaluations. Our waveform generator (M2p.6531-x4) lacks the sample rate necessary to generate 13 MHz signals. As a workaround, we used a Siglent signal generator with limited memory, restricting us to transmitting 1000-bit sequences. We tested ten random 1000-bit sequences and observed a bit error rate near zero.

These results suggest that commercial high-frequency AOMs, when repurposed to operate in the Raman-Nath regime, can significantly extend the performance capabilities of our proposed system.
(2) Custom low-cost hardware. In parallel with scaling to high-frequency AOMs, another promising direction is the development of low-cost, task-specific waveform generators. Our LUT-based synthesis shows that signals are highly compressible: repeated patterns map to identical stored values rather than slightly differing floating-point samples, enabling compact storage and efficient playback. Because the transmitter needs only a small lookup table per codeword, a dedicated generator built from inexpensive direct-digital-synthesis (DDS) ICs (e.g., AD9833/AD9851/AD9102) can be realized with a bill of materials under $50. Such resource-efficient hardware could replace bulky laboratory instruments and pave the way toward compact, long-term deployable systems.

(3) Joint waveform and error-correcting code design. In this work, we employed 3-bit redundancy to induce approximately quadratic and inverse-quadratic refractive index profiles, thereby enhancing optical contrast and reducing the bit error rate (BER). While effective, this approach reduces the net data rate by a factor of three. A promising direction for future research is the joint design of optimal waveforms and error-correcting codes in a mathematically rigorous framework. Such a co-design strategy could enable higher bitrates without compromising transmission accuracy, offering fundamental improvements to backscatter communication systems that are independent of transducer frequency.
(4) Multi-node extensions. Another important challenge is scaling beyond point-to-point links to support multiple assets. One possible approach is to employ high-power wide-beam illumination with omnidirectional photodetectors, while separating concurrent signals through frequency- or time-division assignments of acoustic transducers or lightweight handshake protocols. More sophisticated approaches may use adaptive coding and synchronization, ultimately enabling cooperative backscatter networks for multi-agent sensing and communication.
(5) Testing on underwater and aerial drones. Finally, addressing mechanical constraints and deploying the system on real underwater or aerial drones for tasks such as exploration, environmental monitoring, infrastructure inspection, and search-and-rescue operations represents an important avenue for future work.

Overall, our work establishes a foundation for high-speed acousto-optic backscatter communication, demonstrating its feasibility in controlled settings and exposing the key hurdles that remain for real deployments. By tackling these challenges—through advances in mechanical design, custom hardware, coding strategies, and multi-node networking—the technique can evolve from a research prototype into a practical enabler of large-scale underwater sensing and communication.

Acknowledgments

We are grateful to Ioannis Gkioulekas (Carnegie Mellon University) and Devin J. Balkcom (Dartmouth College) for lending resources for experiments. This work was supported in part by the NSF under Grants No. 2326904, 2144624 and 1552924. ChatGPT is used for manuscript refinement and Meta's Llama for generating images.

References

Shlomi Arnon. 2010. Underwater optical wireless communication network. *Optical Engineering* 49, 1 (2010), 015001.

Rens Bloom, Marco Zúñiga Zamalloa, and Chaitra Pai. 2019. LuxLink: Creating a wireless link from ambient light. In *Proceedings of the 17th conference on embedded networked sensor systems*. 166–178.

Charles J Carver, Qijia Shao, Samuel Lensgraf, Amy Sniffen, Maxine Perroni-Scharf, Hunter Gallant, Alberto Quattrini Li, and Xia Zhou. 2022. Sunflower: locating underwater robots from the air. In *Proceedings of the 20th annual international conference on mobile systems, applications and services*. 14–27.

Carver J Carver, Zhao Tian, Hongyong Zhang, Kofi M Odame, Alberto Quattrini Li, and Xia Zhou. 2020. AmphiLight: Direct Air-Water Communication with Laser Light. In *USENIX Symposium on Networked Systems Design and Implementation (NSDI)*.

Maysamreza Chamanzar, Matteo Giuseppe Scopelliti, Julien Bloch, Ninh Do, Minyoung Huh, Dongjin Seo, Jillian Iafrati, Vikaas S Sohal, Mohammad-Reza Alam, and Michel M Maharbiz. 2019. Ultrasonic sculpting of virtual optical waveguides in tissue. *Nature communications* 10, 1 (2019), 1–10.

Jun Chen, Chunlong Fei, Danmei Lin, Pengkai Gao, Junshan Zhang, Yi Quan, Dongdong Chen, Di Li, and YinTang Yang. 2022. A review of ultrahigh frequency ultrasonic transducers. *Frontiers in Materials* 8 (2022), 733358.

Xiaoyang Chen, Kwok Ho Lam, Ruimin Chen, Zeyu Chen, Ping Yu, Zhongping Chen, K Kirk Shung, and Qifa Zhou. 2017. An adjustable multi-scale single beam acoustic tweezers based on ultrahigh frequency ultrasonic transducer. *Biotechnology and Bioengineering* 114, 11 (2017), 2637–2647.

Maxim N Cherkashin, Carsten Brenner, Georg Schmitz, and Martin R Hofmann. 2020. Transversally travelling ultrasound for light guiding deep into scattering media. *Communications Physics* 3, 1 (2020), 1–11.

Mandar Chitre, Shiraz Shahabudeen, and Milica Stojanovic. 2008. Underwater acoustic communications and networking: Recent advances and future challenges. *Marine Technology Society Journal* 42, 1 (2008), 103.

Hyun-Taek Choi and Junku Yuh. 2016. Underwater robots. In *Springer Handbook of Robotics*. Springer, 595–622.

John E Damuth and Hilary Clement Olson. 2001. Neogene-Quaternary contourite and related deposition on the West Shetland Slope and Faeroe-Shetland Channel revealed by high-resolution seismic studies. *Marine Geophysical Researches* 22 (2001), 369–398.

Martí Duocastella, Salvatore Surdo, Alessandro Zunino, Alberto Diaspro, and Peter Saggau. 2020. Acousto-optic systems for advanced microscopy. *Journal of Physics: Photonics* 3, 1 (2020), 012004.

Aline Eid, Jack Rademacher, Waleed Akbar, Purui Wang, Ahmed Allam, and Fadel Adib. 2023. Enabling long-range underwater backscatter via van atta acoustic networks. In *Proceedings of the ACM SIGCOMM 2023 Conference*. 1–19.

Seyed Keyarash Ghiasi, Marco A Zúñiga Zamalloa, and Koen Langendoen. 2021. A principled design for passive light communication. In *Proceedings of the 27th Annual International Conference on Mobile Computing and Networking*. 121–133.

Seyed Keyarash Ghiasi and Marco Zuniga. 2024. Exploiting Polarization and Color to Enable MIMO Backscattering with Light. In *Proceedings of the 22nd ACM Conference on Embedded Networked Sensor Systems*. 771–783.

Camila MG Gussen, Paulo SR Diniz, Marcello LR Campos, Wallace A Martins, Felipe M Costa, and Jonathan N Gois. 2016. A survey of underwater wireless communication technologies. *J. Commun. Inf. Sys* 31, 1 (2016), 242–255.

Robert Headrick and Lee Freitag. 2009. Growth of underwater communication technology in the US Navy. *IEEE Comm. Mag.* 47, 1 (2009), 80–82.

Dawoon Jeong, Hansol Jang, Min Uk Jung, and Chang-Seok Kim. 2022. Angular Resolution Variable FMCW LiDAR with Acousto-Optic Deflector. In *Imaging Systems and Applications*. Optica Publishing Group, ITh4D–3.

SeungYeon Kang, Martí Duocastella, and Craig B Arnold. 2020. Variable optical elements for fast focus control. *Nature Photonics* 14, 9 (2020), 533–542.

Yasin Karimi, Matteo Giuseppe Scopelliti, Ninh Do, Mohammad-Reza Alam, and Maysamreza Chamanzar. 2019. In situ 3D reconfigurable ultrasonically sculpted optical beam paths. *Optics Express* 27, 5 (2019), 7249–7265.

Hemani Kaushal and Georges Kaddoum. 2016. Underwater optical wireless communication. *IEEE Access* 4 (2016), 1518–1547.

Mohammad-Ali Khalighi, Chadi Gabriel, Tasnim Hamza, Salah Bourennane, Pierre Leon, and Vincent Rigaud. 2014. Underwater wireless optical communication; recent advances and remaining challenges. In *2014 16th International Conference on Transparent Optical Networks (ICTON)*. IEEE, 1–4.

Jiangtao Li, Angli Liu, Guobin Shen, Liqun Li, Chao Sun, and Feng Zhao. 2015. Retro-VLC: Enabling Battery-free Duplex Visible Light Communication for Mobile and IoT Applications. In *Proceedings of the 16th International Workshop on Mobile Computing Systems and Applications* (Santa Fe, New Mexico, USA) *(HotMobile '15)*. Association for Computing Machinery, New York, NY, USA, 21–26. doi:10.1145/2699343.2699354

Gang Ma, Muhammad Hanis Kamaruddin, Hooi-Siang Kang, Pei-Sean Goh, Moo-Hyun Kim, Kee-Quen Lee, and Cheng-Yee Ng. 2021. Watertight integrity of underwater robotic vehicles by self-healing mechanism. *Ain Shams Engineering Journal* 12, 2 (2021), 1995–2007.

Curtis D Mobley. 2010. Optical properties of water. *Handbook of optics* 4 (2010), 1–1.

Nazish Naeem, Jack Rademacher, Ritik Patnaik, Tara Boroushaki, and Fadel Adib. 2024. SeaScan: An Energy-Efficient Underwater Camera for Wireless 3D Color Imaging. In *Proceedings of the 30th Annual International Conference on Mobile Computing and Networking*. 785–799.

Jin-Ping Niu and Geoffrey Ye Li. 2019. An Overview on Backscatter Communications. *Journal of Communications and Information Networks* 4, 2 (2019), 1–14. doi:10.23919/JCIN.2019.8917868

Olushola Olufemi Odeyemi and Peter Adeniyi Alaba. 2025. Efficient and reliable corrosion control for subsea assets: challenges in the design and testing of corrosion probes in aggressive marine environments. *Corrosion Reviews* 43, 1 (2025), 79–126.

Adithya Pediredla, Srinivasa G Narasimhan, Maysamreza Chamanzar, and Ioannis Gkioulekas. 2023a. Megahertz Light Steering Without Moving Parts. In *Proceedings of the IEEE/CVF Conference on Computer Vision and Pattern Recognition*. 1–12.

Adithya Pediredla, Matteo Giuseppe Scopelliti, Srinivasa Narasimhan, Maysamreza Chamanzar, and Ioannis Gkioulekas. 2023b. Optimized virtual optical waveguides enhance light throughput in scattering media. *Nature Communications* 14, 1 (2023), 5681.

Yvan R Petillot, Gianluca Antonelli, Giuseppe Casalino, and Fausto Ferreira. 2019. Underwater robots: From remotely operated vehicles to intervention-autonomous underwater vehicles. *IEEE Robot. Autom. Mag.* 26, 2 (2019), 94–101.

Alexander B Phillips, Robert Templeton, Daniel Roper, Richard Morrison, Miles Pebody, Philip M Bagley, Rachel Marlow, Ed Chaney, James Burris, Alberto Consensi, et al. 2023. Autosub Long Range 1500: A continuous 2000 km field trial. *Ocean Engineering* 280 (2023), 114626.

Alberto Quattrini Li, Charles J Carver, Qijia Shao, Xia Zhou, and Srihari Nelakuditi. 2023. Communication for Underwater Robots: Recent Trends. *Current Robotics Reports* 4, 2 (2023), 13–22.

Sihua Shao, Abdallah Khreishah, and Issa Khalil. 2018. RETRO: Retroreflector based visible light indoor localization for real-time tracking of IoT devices. In *IEEE INFOCOM 2018-IEEE Conference on Computer Communications*. IEEE, 1025–1033.

Ying Shen, Chuanjiang Zhao, Yu Liu, Shu Wang, and Feng Huang. 2021. Underwater optical imaging: Key technologies and applications review. *IEEE Access* 9 (2021), 85500–85514.

Dhawal Sirikonda, Praneeth Chakravarthula, Ioannis Gkioulekas, and Adithya Pediredla. 2025. Structured light with a million light planes per second . *IEEE Transactions on Pattern Analysis & Machine Intelligence* 01 (Aug. 2025), 1–13. doi:10.1109/TPAMI.2025.3599143

Raymond C Smith and Karen S Baker. 1981. Optical properties of the clearest natural waters (200–800 nm). *Applied optics* 20, 2 (1981), 177–184.

Miguel Chávez Tapia, Talia Xu, Zehang Wu, and Marco Zúñiga Zamalloa. 2022. SunBox: Screen-To-camera communication with ambient light. *Proceedings of the ACM on Interactive, Mobile, Wearable and Ubiquitous Technologies* 6, 2 (2022), 1–26.

Francesco Tonolini and Fadel Adib. 2018. Networking across boundaries: enabling wireless communication through the water-air interface. In *Proceedings of the 2018 Conference of the ACM Special Interest Group on Data Communication*. 117–131.

Chen S Tsai. 2013. *Guided-wave acousto-optics: interactions, devices, and applications*. Vol. 23. Springer Science & Business Media.

Michael Unser. 1999. Splines: A perfect fit for signal and image processing. *IEEE Signal processing magazine* 16, 6 (1999), 22–38.

Zahra Vali, Asghar Gholami, Zabih Ghassemlooy, Masood Omoomi, and David G Michelson. 2018. Experimental study of the turbulence effect on underwater optical wireless communications. *Applied optics* 57, 28 (2018), 8314–8319.

Purui Wang, Lilei Feng, Guojun Chen, Chenren Xu, Yue Wu, Kenuo Xu, Guobin Shen, Kuntai Du, Gang Huang, and Xuanzhe Liu. 2020. Renovating road signs for infrastructure-to-vehicle networking: A visible light backscatter communication and networking approach. In *Proceedings of the 26th Annual International Conference on Mobile Computing and Networking*. 1–13.

Yanxiang Wang, Yiran Shen, Kenuo Xu, Mahbub Hassan, Guangrong Zhao, Chenren Xu, and Wen Hu. 2024. Towards high-speed passive visible light communication with event cameras and digital micro-mirrors. In *Proceedings of the 22nd ACM Conference on Embedded Networked Sensor Systems*. 704–717.

Tsai-Chen Wu, Yu-Chieh Chi, Huai-Yung Wang, Cheng-Ting Tsai, and Gong-Ru Lin. 2017. Blue laser diode enables underwater communication at 12.4 Gbps. *Scientific reports* 7, 1 (2017), 40480.

Yue Wu, Purui Wang, and Chenren Xu. 2019. Improving visible light backscatter communication with delayed superimposition modulation. In *The 25th Annual International Conference on Mobile Computing and Networking*. 1–3.

Yue Wu, Purui Wang, Kenuo Xu, Lilei Feng, and Chenren Xu. 2020. Turboboosting visible light backscatter communication. In *Proceedings of the Annual conference of the ACM Special Interest Group on Data Communication on the applications, technologies, architectures, and protocols for computer communication*. 186–197.

Kenuo Xu, Chen Gong, Bo Liang, Yue Wu, Boya Di, Lingyang Song, and Chenren Xu. 2022a. Low-latency visible light backscatter networking with RetroMUMIMO. In *Proceedings of the 20th ACM Conference on Embedded Networked Sensor Systems*. 448–461.

Kenuo Xu, Kexing Zhou, Chengxuan Zhu, Shanghang Zhang, Boxin Shi, Xiaoqiang Li, Tiejun Huang, and Chenren Xu. 2023. When Visible Light (Backscatter) Communication Meets Neuromorphic Cameras in V2X. In *Proceedings of the 24th International Workshop on Mobile Computing Systems and Applications*. 42–48.

Talia Xu, Miguel Chávez Tapia, and Marco Zúñiga. 2022b. Exploiting Digital Micro-Mirror Devices for Ambient Light Communication. In *19th USENIX Symposium on Networked Systems Design and Implementation (NSDI 22)*. 387–400.

Xieyang Xu, Yang Shen, Junrui Yang, Chenren Xu, Guobin Shen, Guojun Chen, and Yunzhe Ni. 2017. PassiveVLC: Enabling Practical Visible Light Backscatter Communication for Battery-free IoT Applications. In *Proceedings of the 23rd Annual International Conference on Mobile Computing and Networking* (Snowbird, Utah, USA) *(MobiCom '17)*. Association for Computing Machinery, New York, NY, USA, 180–192. doi:10.1145/3117811.3117843

Seok Pyo Yoon, Sung-Ho Jeong, Dong Kyun Kim, Seong-yeol Yoo, Bong-Huan Jun, Jong-Boo Han, Hyungwoo Kim, and Hyung Taek Ahn. 2024. Optimal Attitude Determination for the CR200 Underwater Walking Robot. *Applied Sciences* 14, 23 (2024), 11027.